energies

Article

Surrogate Model for Design Uncertainty Estimation of Nonlinear Electromagnetic Vibration Energy Harvester

Marcin Kulik *, Rafał Gabor and Mariusz Jagieła

Faculty of Electrical Engineering, Automatic Control and Informatics, Opole University of Technology, Proszkowska 76, 45-758 Opole, Poland
* Correspondence: m.kulik@po.edu.pl

Abstract: The paper proposes a solution to the problem of estimating the uncertainty of the output power with respect to the design parameters for an electromagnetic vibration energy harvesting converter. Due to costly utilisation of time-domain mathematical models involved in the procedure of determination of the average output power of the system, an algorithm for developing the surrogate model that enables rapid estimation of this quantity within the prescribed frequency band limits is proposed. As a result, the metamodel sensitive to the most impactful design parameters is developed using Kriging with successive refinement of the design grid for gaining the accuracy. Under operational conditions with a constant magnitude of the acceleration signal and the prescribed frequency band limits, the surrogate model enables evaluation of the average output power of the system at 10^5 design points in less than 2 s of computer execution time. The consistency and accuracy of the results obtained from the surrogate model is confirmed by comparison of selected results of computations with measurements carried out on the manufactured prototype. Based on the latter and the surrogate model, the confidence intervals for the design procedure were determined and the most important spread quantities were estimated, providing quantitative information on the accuracy of the design procedure developed for the considered system.

Keywords: energy harvesting; electromagnetic transducer; nonlinear resonance; kriging; uncertainty analysis

Citation: Kulik, M.; Gabor, R.; Jagieła, M. Surrogate Model for Design Uncertainty Estimation of Nonlinear Electromagnetic Vibration Energy Harvester. *Energies* **2022**, *15*, 8601. https://doi.org/10.3390/en15228601

Academic Editors: Syed Kamrul Islam and Salvatore Pullano

Received: 18 October 2022
Accepted: 15 November 2022
Published: 17 November 2022

1. Introduction

The unification of the real world of industrial machines with the virtual world, which is the concept of Industry 4.0, makes it possible to reduce production costs and flexibly respond to individual customer needs [1,2]. To be able to realise the assumptions of Industry 4.0, it is necessary, among other problems, to equip manufacturing machines with intelligent automation components (drives, sensors, data processing systems, etc.) [3]. Undoubtedly, this modern type of production, based on digital technologies, contributes to an increase in demand for electrical energy, which, so far, is mostly obtained from conventional energy sources. Solving the problem of maintaining energy sustainability is a challenge even for Industry 4.0 but is also specified for the 5.0 technology, which emphasises the importance of research and innovation in supporting the industry in its long-term service for humanity [4]. The energy crisis and environmental pollution caused by greenhouse gases have prompted researchers to conduct research on harvesting alternative energy sources. It has been shown that harvesting energy directly from the surrounding environment under the influence of mechanical vibrations, heat, fluid flows, and electromagnetic radiation in the form of light and radio frequency (RF) waves can provide clean energy to operate various electronic devices [5–8].

In the literature, major attention is paid to systems that convert mechanical energy, which can be obtained and effectively converted into useful electrical energy [9–14]. The transducers using piezoelectric, magnetostrictive, magnetoelectric, electrostatic or electromagnetic phenomena allow conversion of energy of vibrations generated during operation of industrial machinery, vehicle movement or human activity [15–18].

The small dimensions of mini-generators require a customised approach to their design, often balancing on the edge of full utilisation of materials. In the process of designing such converters, the optimisation algorithms are used to choose the material and to receive the information on geometric and load parameters for given requirements. However, one should be aware that the actual performance of the modelled object is always subject to uncertainties with respect to the expected values of parameters (i.e., dimensions, masses, strengths) [19,20]. This is one of the most important reasons for the engagement of probabilistic models in the process of designing.

The literature distinguishes the three types of uncertainty that are particularly important for engineering analysis, namely: errors, imprecision, and instability [21]. Many publications have attempted to explain the meaning of uncertainty and to provide its classification [22–24]. As stated in [25], uncertainty can be caused by lack or excess of information, conflicting evidence, measurement uncertainty, ambiguity and/or subjectivity. The stochastic parameters of the object manifest an inherent uncertainty due to material properties and also due to unexpected occurrence of physical processes.

Accurate assessment of design uncertainty requires the use of the computer simulation-based analyses, bounding techniques or the use of the mentioned probabilistic models [26–28]. These computer simulation-based analyses are based on the solution of coupled mechanical-electrical problems described by large coupled system ordinary differential equations, later called a full model. The analyses allowing for determination of design uncertainty generally require a very large number of operating points to be considered, which makes them computationally intensive or even impossible to realise within an acceptable time range. The latter applies especially to the nonlinear systems whose frequency characteristics are non-smooth functions that expose features such as amplitude jump and hysteresis [29] and which cannot be approximated using simple empirical models. However, their determination within a prescribed frequency range is crucial for every design. Until the present, the literature has reported on the uncertainty estimation problem for various linear or weakly nonlinear systems including piezoelectric energy harvesters [20,27,30]. In many cases the models of these systems can be represented by empirical models or approximated in selected operating points by the linear models. This is, however, not the case for the nonlinear system considered in this work.

Basically, the frequency characteristics of nonlinear vibration energy harvesters can be determined in two ways, namely by numerical solution of a system of ordinary differential equations using time-stepping solver [31,32] or by applying the harmonic balance approach [33]. Both methods have advantages and drawbacks that have already been discussed in [34,35]. For the systems whose equations are formulated as a strongly or weakly coupled problem at the finite element level, as one considered in this work, application of the latter technique is a serious challenge and may even lead to impractical results. The time-stepping method is simpler and more universal, although its application in determination of the frequency characteristics requires massive computer execution time. This has created a motivation for the authors to search for the possibility of realising such task.

The structure and the operating principle of the considered electromagnetic vibration energy harvester with nonlinear resonance are presented in Section 2. In Section 3, a detailed mathematical formulation of the full model is presented. The procedure of developing the metamodel and its implementation for the design uncertainty analysis involving the most important quantity of the system, namely the output power, is described in Section 4.

Based on the metamodel, the design uncertainty analysis of the system under consideration is estimated within the prescribed frequency band limits where the system was designed to operate. Further analyses in Section 4, based on the comparison of results of computer simulations with those measured on the physical system, enabled determination of the manufacturing tolerances for the physical system.

In this paper, the authors present an algorithm for creating a Kriging metamodel [36,37] of the considered energy harvester suitable for estimation of power generated within the prescribed frequency band limits with computational costs reduced by a factor of a few hundred with respect to the fully coupled nonlinear model. The new knowledge presented in the paper is related mainly to the development and implementation of an algorithm for creation of the surrogate model for a highly nonlinear energy harvesting system. In particular, it has been shown how the frequency dependence of the quantities of interest, such as the output power, can be incorporated into the metamodel. Through the comparison of selected results of computations with ones obtained from measurements on the laboratory test-stand, it has also been demonstrated that the sensitivity of the created surrogate model to the most influential design parameters is very similar to that of the physical system.

2. Considered Nonlinear Electromagnetic Energy Harvester

The operation of the presented Electromagnetic Energy Harvester has already been discussed in publications [31,38] and in a patent [39]. The system was designed with the aim to work as a part of an autonomous power supply in a wireless sensor network. Its frequency characteristic is fitted best to the sources of vibrations with chirp-like frequency-amplitude characteristics of the vibrations signal. These sources are, e.g., accelerating and decelerating drive systems of industrial pumps and compressors, vibrating tables for concrete slabs or internal combustion engines.

A schematic diagram of the kinematic system of the nonlinear electromagnetic mini-generator is shown in Figure 1. Mathematically, the system can be described by the following equation of balance of forces

$$ma + F_d + \left[k + k_{mag}(\zeta)\right]\zeta(t) = ma_{vib}(t) - mg - F_e(t), \tag{1}$$

$$a_{vib}(t) = a_{rms}\sqrt{2}\, sin(2\pi f t), \tag{2}$$

where: m—mass of the vibrating part, a—acceleration of the vibrating part, F_d—damping force, k—stiffness coefficient, k_{mag}—stiffness coefficient from the magnetic force, ζ—displacement of the vibrating part, a_{vib}—external vibration acceleration, a_{rms}—rms value of vibration acceleration, f—vibration frequency, F_e—electromagnetic force, g—gravity constant.

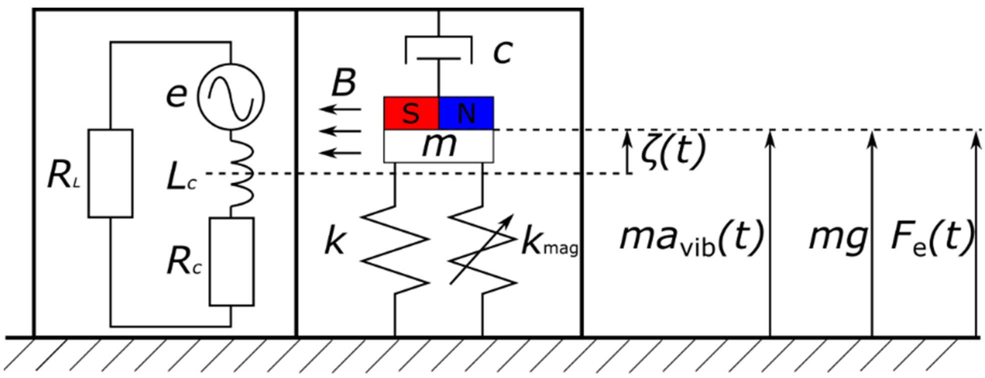

Figure 1. Schematic diagram of the kinematic system of an electromagnetic system for energy harvesting from mechanical vibrations with additional nonlinear magnetic stiffness k_{mag}. B—magnetic flux density, c—damping ratio; e—induced voltage; L_c—coil inductance; R_c—coil resistance; R_L—load resistance.

The nonlinear magnetic stiffness is obtained by division of the magnetic force by ζ

$$k_{mag}(\zeta) = \frac{F_{mag}(\zeta)}{\zeta} \tag{3}$$

The CAD model and manufactured prototype of the considered structure of the Electromagnetic Energy Harvester are shown in Figure 2. A crucial structural element of the mini-generator is a flat beam spring attached to the housing on one end and to the yokes with permanent magnets on the other. The system is attached directly to the vibration source, which causes mutual displacement of permanent magnets embedded in yokes, with respect to the stationary coils attached to the system on the outer sidewalls of the yokes. As a result of the interaction of the magnets, a variable magnetic flux is generated in the coils, which induces the electromotive force in coils [31]. An important design problem to solve in this type of system is to potentially obtain a wide band of the operating frequency. One of the ways to achieve this goal is to use a nonlinear oscillator. The system considered in this paper belongs to such a family of converters. The nonlinear resonance in the considered system occurs due to the existence of an internal magnetic force F_{mag} (see Figure 1) caused by the interaction of moving permanent magnets on yokes with additional permanent magnets [29,31]. The stationary permanent magnets were placed in a vertical support located between the yokes as shown in Figure 2a [39].

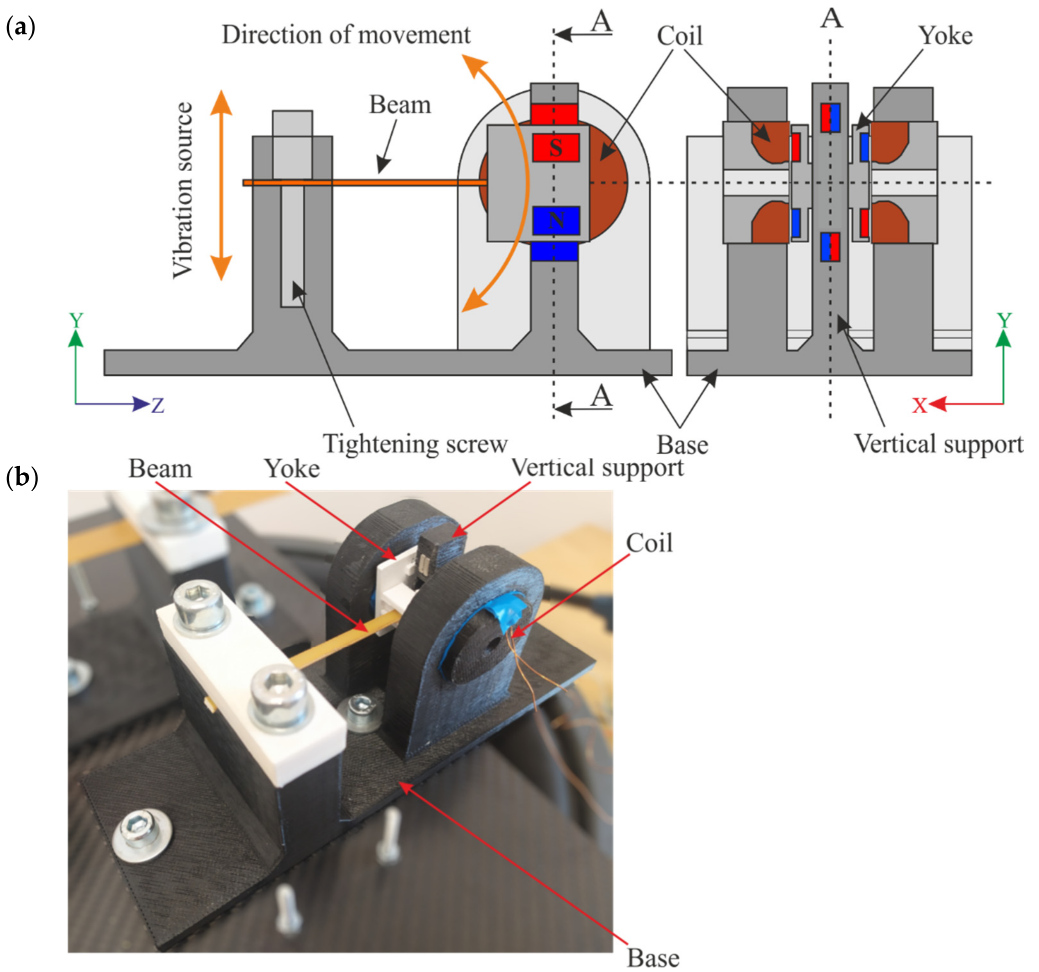

Figure 2. *Cont.*

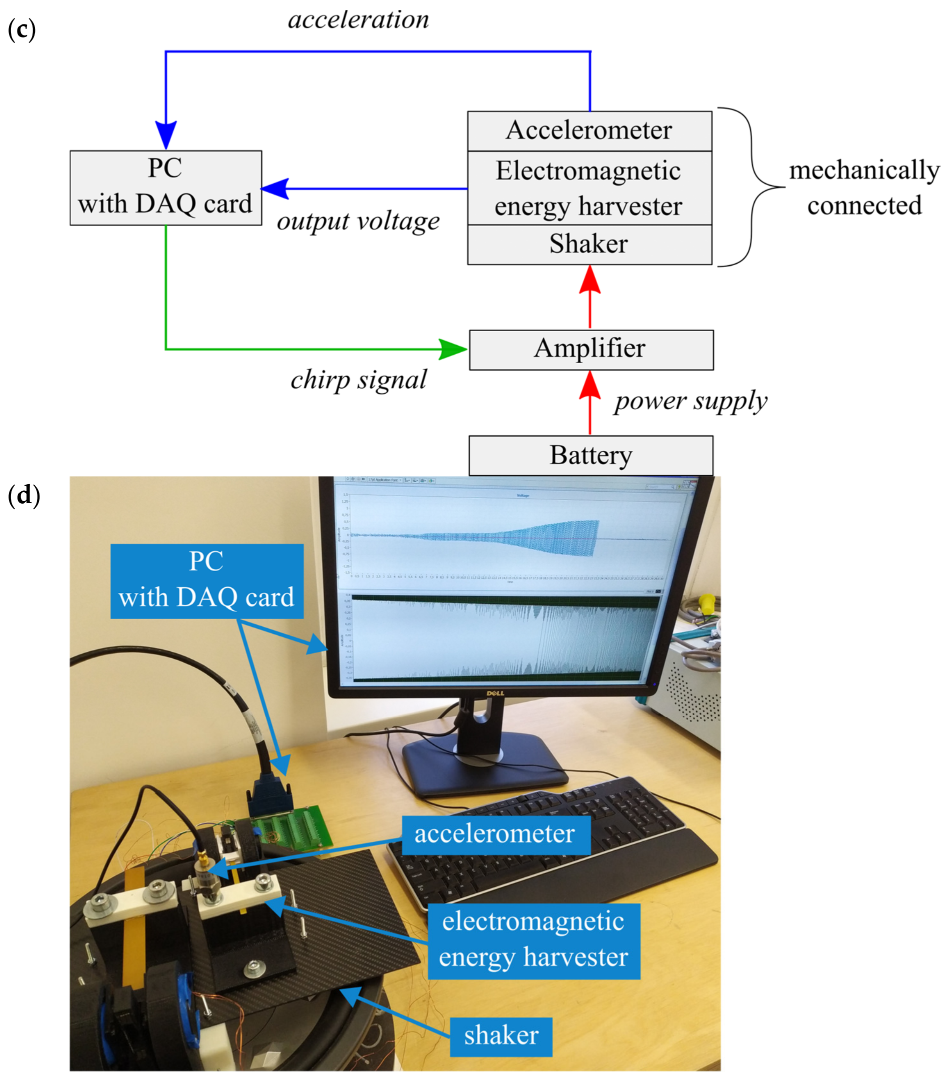

Figure 2. (**a**) CAD diagram of nonlinear system vibration energy harvester using electromagnetic mini-generator; (**b**) physical model on laboratory test-stand; (**c**) schematic diagram of a test-stand and (**d**) photograph of a test-stand.

3. Mathematical Model

The prototype of the presented converter was manufactured based on optimisation for maximum output power carried out in [38]. The optimised variables were the number of turns, the length of the active part of the coil, the cross-sectional diameter of the wire, and the load resistance of the step-up voltage converter. The problem of maximising the output power was solved using a sequentially refined surrogate employing Kriging [38,40]. In the process of optimising the converter dimensions, the fact that each turn of the coil winding is treated separately using appropriate formulas derived using integral laws plays a crucial role, making it possible to simultaneously optimise the placement of each turn for maximum turn voltage and also minimise the coil resistance by selecting only the turns with largest contribution to the output voltage.

In order to analyse the mechanical vibration energy conversion system in detail, the original computer models were developed to help determine the magnetic flux linking with the coil, the variation of magnetic force F_{mag}, and the displacement of the mechanical part in response to the forces imposed.

3.1. Physical Quantities of Electric Circuit

Due to the large inhomogeneity of the magnetic field distribution around the active elements of the coil, the accuracy of calculation of the magnetic flux linkage, assuming a 2d flux distribution across the coil cross section, is negatively affected by field fringes around the peripheral regions. A similar error occurs in the calculation of the inductance of the coil having the curvilinear parts. For this reason, the 3d model is used here, and the equations describing the quantities required by the design routine are presented below.

Assuming geometrical symmetry of the system with respect to the *yz* plane in Figure 3a, only the component of magnetic flux density perpendicular to the surface bounded by a single coil (the surface parallel to the *yz* plane) contributes to coil magnetic flux. This component at any distance from a perpendicular permanent magnet, with the direction of magnetisation consistent with the *x*-axis, can be determined from the formula [41,42]

$$B_x = \frac{\mu_0}{4\pi}\int_{S+}\frac{3(x-x')M_{\mu x}}{|r-r'|^3}ds - \frac{\mu_0}{4\pi}\int_{S-}\frac{3(x-x')M_{\mu x}}{|r-r'|^3}ds, \tag{4}$$

where $M_{\mu x}$ is the component of the magnetisation vector in x direction, μ_0 is the vacuum permeability, whilst $\boldsymbol{r}$, $\boldsymbol{r}'$ are the source and observation points, and S+, S− are the magnet surfaces parallel to the *yz* plane. The formula describes the contribution to B_x due to a single magnet. The total value is obtained through summation of the contributions from all moving magnets.

Because the quantity of interest for the design routine is the derivative of the flux linkage vs. ζ, and not the flux linkage itself, thanks to Green's theorem [43], the former can easily be computed using the line integral. This quantity can be obtained as

$$\frac{\partial\lambda(\zeta)}{\partial\zeta} = \frac{\partial}{\partial\zeta}\iint B_x dydz = -\oint B_x dz. \tag{5}$$

The line integral is computed numerically along the contour of each turn within the coil.

The resistance R_c and inductance L_c for a coil composed of separate turns is obtained from analytical formulas [44–46]. For the coil with the assumed racetrack-like shape shown in Figure 3a, the expressions describing the resistance and inductance of the coil are obtained by superposition, respectively, of the resistance and inductance coefficients for rectilinear segments of length l_z and the half-circle segments. The complete formula for the resistance of a coil can be written as follows:

$$R_c = n_z\frac{2l_z}{\sigma_{\mathrm{Cu}}\pi {r_d}^2} + \sum_{i=1}^{n_z}\frac{2\pi r_{c,i}}{\sigma_{\mathrm{Cu}}\pi {r_d}^2}, \tag{6}$$

where n_z is a number of concentric circular loops in a composed coil, σ_{Cu} is copper conductivity and r_d is the radius of a coil turn. In calculating the inductance of the coil, the self- and mutual inductance of the turns must be taken into account

$$L_c = \sum_{i=1}^{n_z} L_{r,i} + n_z L_z + \sum_{i=1}^{n_z}\sum_{j=1}^{n_z} M_{z,ij} + \sum_{i=1}^{n_z}\sum_{j=1}^{n_z} M_{r,ij}. \tag{7}$$

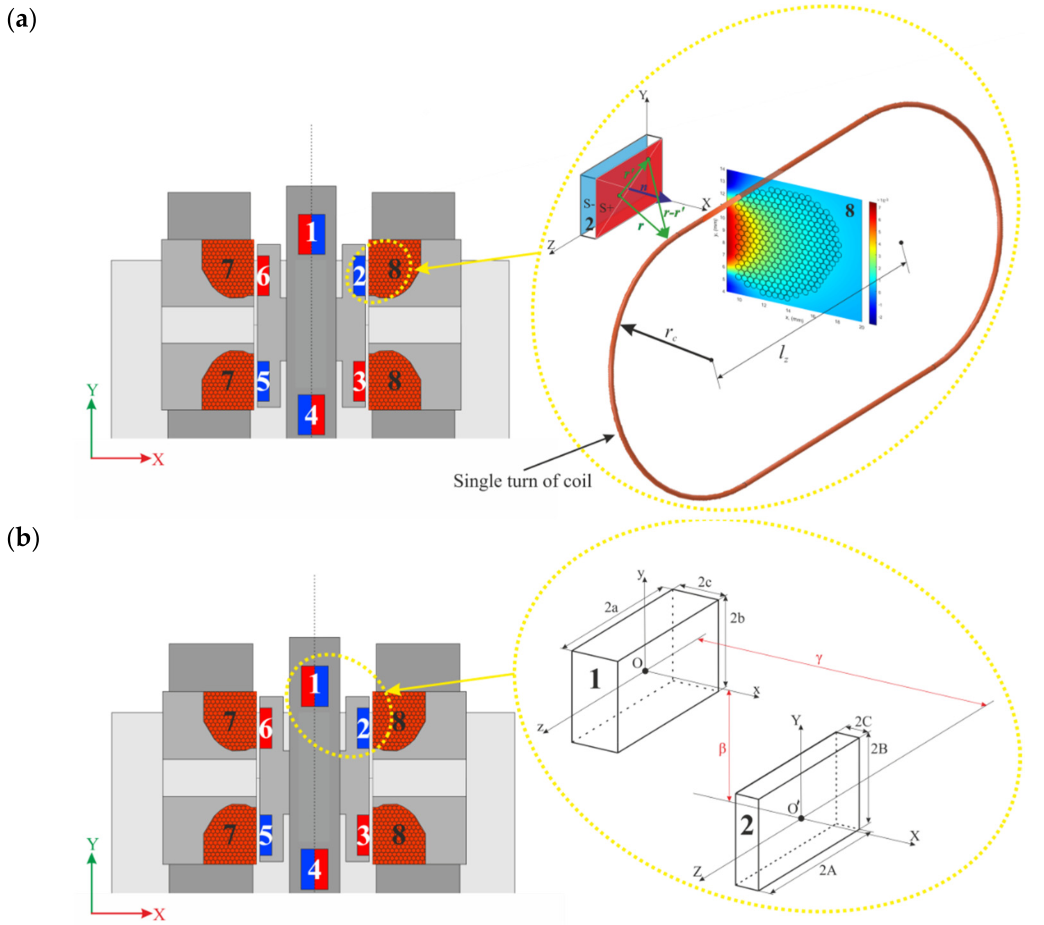

Figure 3. Schematic diagram illustrating the magnetic field computation strategy for calculations of: (**a**) magnetic flux derivative for each coil turn, (**b**) magnetic force between permanent magnets. 1, 4—magnets in vertical support, 2, 3, 5, 6—magnets in yokes, 7, 8—windings, l_z—length of rectilinear coil turn segments; r_c—radius of curved coil turn segments, 2a, 2b, 2c—the magnet (located in Vertical support) dimensions; 2A, 2B, 2C—magnet dimensions (located in yoke), O, O'—geometrical centres of magnets, β, γ—distances between magnets.

For a single coil, the self-inductance of the end connections L_r, the self-inductance of the active parts L_z, the mutual inductance of the active parts M_z and the mutual inductance of the end connections M_r are determined from the following formulas:

$$L_{r,i} = \mu_0 r_{c,i}\left(\ln\frac{8r_{c,i}}{r_d} - 2\right), \tag{8}$$

$$L_z = \frac{\mu_0}{\pi}\left(l_z \ln\frac{\sqrt{2\left({l_z}^2 + {r_d}^2\right)}}{r_d} - \sqrt{{l_z}^2 + {r_d}^2} + r_d\right), \tag{9}$$

$$M_{z,ij} = \frac{\mu_0\left(\left|r_{c,i} - r_{c,j}\right| - \sqrt{{l_z}^2 + \left|r_{c,i} - r_{c,j}\right|^2} + l_z \ln\frac{\sqrt{{l_z}^2 + \left|r_{c,i} - r_{c,j}\right|^2}}{\left|r_{c,i} - r_{c,j}\right|}\right)}{2\pi}, \tag{10}$$

$$M_{r,ij} = \mu_0\sqrt{r_{c,i} r_{c,j}}\left(\left(\frac{2}{\kappa} - \kappa\right)\mathrm{K}(\kappa) - \frac{2}{\kappa}\mathrm{E}(\kappa)\right), \tag{11}$$

$$\kappa = \sqrt{\frac{4r_{c,i} r_{c,j}}{\left(r_{c,i} + r_{c,j}\right)^2 + \left(x_{c,i} - x_{c,j}\right)^2}}. \tag{12}$$

where x_c is the x-coordinate of a single turn, and $\mathrm{K}(\kappa)$ and $\mathrm{E}(\kappa)$ are complete elliptic integrals of the first and second kind, respectively. In the described model, the placement of turns within the coil takes into account the physical distance between the wires so as to consider the insulation thickness.

3.2. Magnetic Force

In order to calculate the frequency characteristics, the magnetic force between the magnets need to be determined as a function of ζ. Assuming uniform distribution of magnetisation on each magnet face and due to the lack of ferromagnetic elements, the magnetic force acting on yokes in y direction can be calculated adopting the formula provided in [47]

$$F_{\mathrm{mag}} = \frac{B_r B_r'}{4\pi\mu_0} \sum_{a=1}^{2} \sum_{b=3}^{6} (-1)^{a+b} F_{\mathrm{ab}}, \tag{13}$$

where B_r and B_r' are the remanences of interacting permanent magnets and F_{ab} is a force between the two parallel faces of the cuboidal magnets (see Figure 3) given by formula

$$F_{ab} = \sum_{i=0}^{1} \sum_{j=0}^{1} \sum_{k=0}^{1} \sum_{l=0}^{1} \sum_{p=0}^{1} \sum_{q=0}^{1} (-1)^{i+j+k+l+p+q} \; \Phi\left(u_{ij}, v_{kl}, w_{pq}, r\right), \tag{14}$$

where:

$$u_{ij} = (-1)^j A - (-1)^i a, \tag{15}$$

$$v_{kl} = \zeta + \beta + (-1)^l B - (-1)^k b, \tag{16}$$

$$w_{pq} = \gamma + (-1)^q C - (-1)^p c, \tag{17}$$

$$r = \sqrt{u_{ij}^2 + v_{kl}^2 + w_{pq}^2}, \tag{18}$$

$$\Phi(u, v, w, r) = \frac{1}{2}\left(u^2 - w^2\right) \log(r - v) + uv \log(r - u) + uw \tan^{-1} \frac{uv}{rw} + \frac{1}{2} rv, \tag{19}$$

and $A, B, C, a, b, c, \beta, \gamma$ are magnet dimensions and distances between magnets, marked in Figure 3b.

3.3. Coupled System of Equations

The mathematical model used in computations combines the equations provided in the previous paragraph with the equations of the distributed parameter dynamic mechanical model of a beam spring. The latter is a 1D finite element model based on Timoshenko's beam theory [48]. The mechanical equations coupled with those describing currents through the coils can be written in the following state–space form

$$\mathbf{E} \frac{d}{dt} \mathbf{X}(t) = \mathbf{A}\mathbf{X}(t) + \mathbf{B}\left(m a_{\mathrm{vib}}(t) - mg - F_{\mathrm{mag}}(\zeta)\right), \tag{20}$$

where:

$$\mathbf{E} = \begin{bmatrix} \mathbf{1} & \mathbf{0} & \mathbf{0}_v \\ \mathbf{0} & \mathbf{M} & \mathbf{0}_v \\ \mathbf{0}_v^{\mathrm{T}} & \mathbf{0}_v^{\mathrm{T}} & L_{\mathrm{c}} \end{bmatrix}_{(4n+1)\ \mathrm{x}\ (4n+1)}, \tag{21}$$

$$\mathbf{X} = \begin{bmatrix} \mathbf{z} \\ \frac{d}{dt}\mathbf{z} \\ i \end{bmatrix}_{(4n+1)\ \mathrm{x}\ 1}, \tag{22}$$

$$\mathbf{A} = \begin{bmatrix} \mathbf{0} & \mathbf{1} & \mathbf{0}_v \\ -\mathbf{K} & -\mathbf{D} & -\mathbf{b}\frac{\partial \lambda(\zeta)}{\partial \zeta} \\ \mathbf{0}_v^{\mathrm{T}} & \mathbf{b}^{\mathrm{T}} \frac{\partial \lambda(\zeta)}{\partial \zeta} & -(R_{\mathrm{L}} + R_{\mathrm{c}}) \end{bmatrix}_{(4n+1)\ \mathrm{x}\ (4n+1)}, \tag{23}$$

$$\mathbf{B} = \begin{bmatrix} \mathbf{0}_v \\ \mathbf{b} \\ 0 \end{bmatrix}_{(4n+1)\ \mathrm{x}\ 1}, \tag{24}$$

n is a number of finite elements of cantilever beam, $\mathbf{M}$, $\mathbf{K}$ are a mass and stiffness matrix, $\mathbf{D} = d_1\mathbf{M} + d_2\mathbf{K}$, is a dampening matrix with $d_1 = 3.4 \times 10^{-5}$, $d_2 = 3.45$ determined experimentally, $\mathbf{z}$ is a column vector of displacements at each point of the discretised beam spring, $\mathbf{b}$ is a sparse column vector connecting variables in $\mathbf{z}$ with end-point displacement along the y-axis, $\mathbf{1}$ is a $2n \times 2n$ identity matrix, $\mathbf{0}$ is a $2n \times 2n$ zero matrix, $\mathbf{0}_v$ is a zero column vector, and i is the current through the coil winding.

The frequency characteristics of the considered system are calculated using a direct time-domain solution of (20) using Matlab ode15s function given the chirp-like excitation signal of acceleration with a duration time of 70 s and frequency bounds between 15 and 50 Hz. The output values of voltage and power are obtained using a moving root–mean-square method.

Because the frequency characteristic of a nonlinear system depends on several parameters, a small variation in one of these parameters can significantly affect the output values. Obtaining this information is crucial for the design to be successful, although the computational effort involved with its extraction using model (20) may lead to an unacceptably long execution time. The possibility of reducing this time is found in replacing the full model by the surrogate [37]. In the next section, an algorithm for developing such a surrogate model is presented.

4. Design Uncertainty and Metamodel

The knowledge of values of all parameters of the system that are taken into account in the design is endowed with some uncertainty [19]. Being aware of the possibility of the occurrence of inaccuracy in fabrication of the individual structural elements of the considered system, a detailed analysis of design parameters was carried out in order to indicate the most impactful ones. The purpose of the analysis was to verify the accuracy in the fabrication of the tested prototype and to determine the reasons for possible differences between the obtained values and theoretical predictions.

4.1. Developing the Metamodel

Table 1 contains the dimensions of the magnetic circuit of the manufactured prototype depicted in Figure 2b.

Table 1. Dimensions of permanents magnets used in energy harvester (see Figure 3).

Dimension	Description	Value
2A	Length of moving permanent magnet	12 (mm)
2B	Height of moving permanent magnet	6 (mm)
2C	Thickness of moving permanent magnet	2 (mm)
2a	Length of fixed permanent magnet	12 (mm)
2b	Height of fixed permanent magnet	6 (mm)
2c	Thickness of fixed permanent magnet	4 (mm)

In the prototype, a single coil (marked as 7, 8 in Figure 3) was wound with 311 turns using a wire with a diameter of 0.35 mm. The length of the straight-line section of the coil (constituting the active part of the coil) is equal to 5.2 mm. The distance between the magnets placed in the yokes (e.g., 2 and 3 or 5 and 6 in Figure 3) in cross-section (y-axis) is equal to 11.4 mm. The distance between stationary magnets placed in vertical support (1 and 4 in Figure 3) relative to the y-axis is equal to 22.1 mm. The distance between the interacting magnets (1 and 2 in Figure 3) with respect to the x-axis is equal to 4.9 mm. The air gap between moving magnets and coils is equal to 1 mm.

Table 2 contains the geometrical and material data of the fibreglass beam spring and permanent magnets used. For each value assigned to a parameter, the standard deviation defining the range of the studies was assigned heuristically based on the knowledge of the manufacturing process and catalogue tolerances of the values of the material data. In addition, a deviation from vibration acceleration was taken into account.

Table 2. Geometrical and material parameters of the system and vibration acceleration with standard deviations.

Parameter	Description	Mean Value μ	Standard Deviation σ
l	Length of cantilever beam	0.046 (m)	0.00005 (m)
t	Thickness of cantilever beam	0.0015 (m)	0.000025 (m)
w	Width of cantilever beam	0.005 (m)	0.00005 (m)
B_r	Remanence	1.4 (T)	0.01 (T)
E	Young's Modulus	15 (GPa)	0.05 (GPa)
m	Mass of yokes with PMs	7.1 (g)	0.05 (g)
a_{RMS}	RMS value of vibration acceleration	[7.5; 10; 12.5] (m/s^2)	0.05 (m/s^2)

An illustration of the effect of variation of the parameters in Table 2 on the performance of the considered system is exhibited in Figures 4–6. The figures show the variations of the magnetic flux derivative and magnetic force as well as the trajectory of the centre of mass of the vibrating yoke.

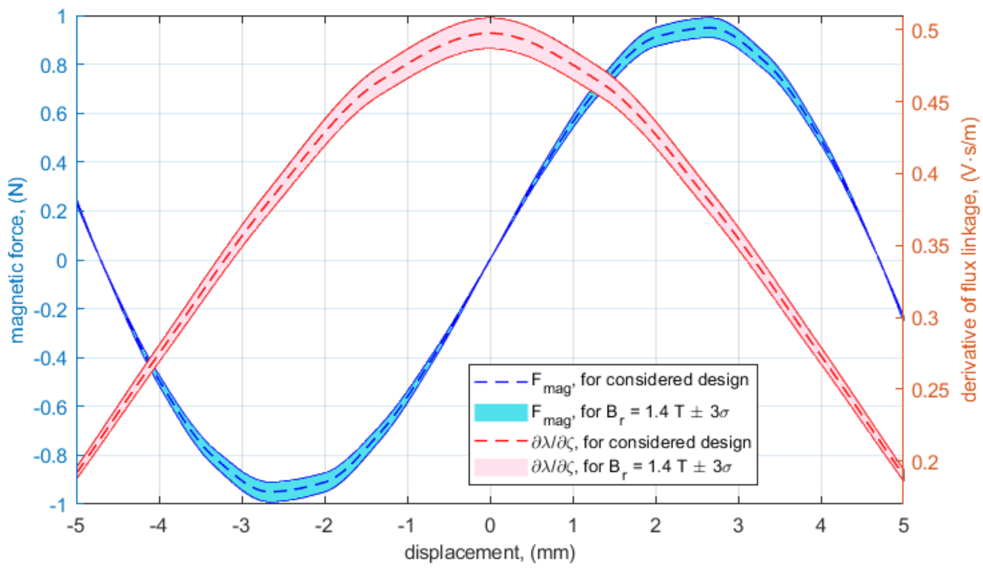

Figure 4. Magnetic force and derivative of flux linkage for three border values of magnet remanence.

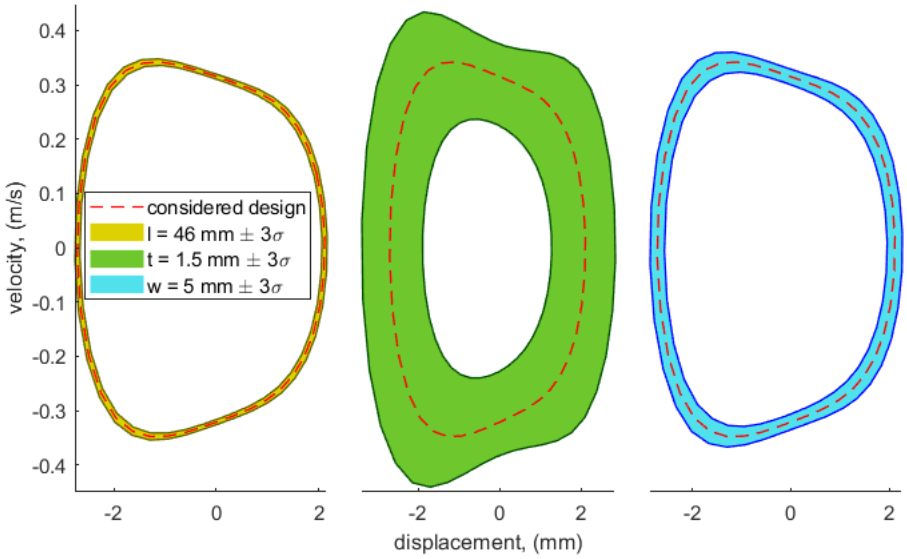

Figure 5. Poincare maps of the centre of mass of a vibrating yoke obtained for three border values of l, t and w (see Table 2). The results are obtained from model (20) for sinusoidal acceleration with a_{RMS} = 12.5 m/s^2 and frequency equal to 25 Hz.

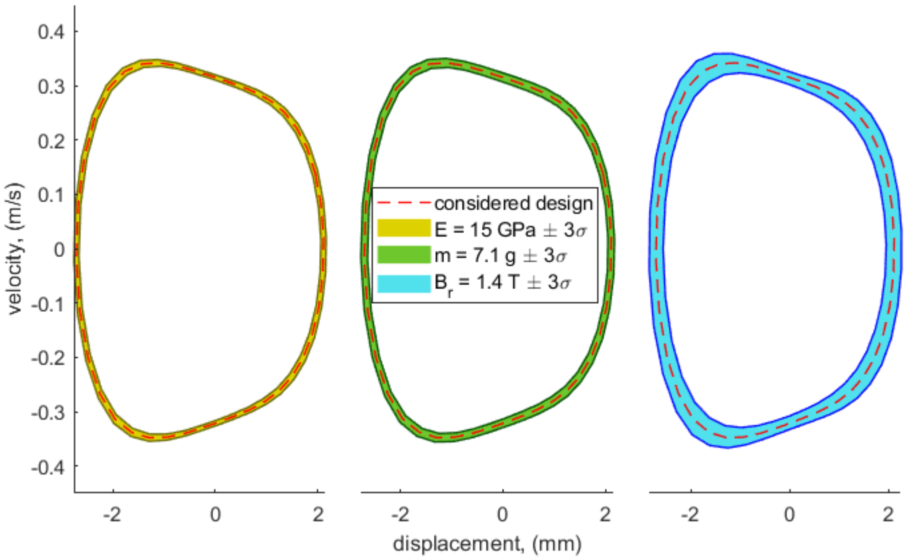

Figure 6. Poincare maps of the centre of mass of a vibrating yoke obtained for three border values of E, m, and B_r (see Table 2). The results are obtained from model (20) for sinusoidal acceleration with a_{RMS} = 12.5 m/s^2 and frequency equal to 25 Hz.

As one can see in the figures, the geometrical parameters of the beam and the value of B_r are the most impactful ones in the system of study.

So far, the separate analyses were carried for selected quantities of the system by varying its selected parameters. In order to estimate the design uncertainty of the system, namely in order to determine the standard deviation of the average power within the considered frequency band, given deviations of the input parameters, it would be necessary to calculate the output power for a huge number of design points (here approximately 10^5 points [30]). The computation of frequency characteristics for the whole cloud of random design points using the full model (20) would lead to unacceptably large computational problems. Therefore, this paper proposes an algorithm to automatically create a low-cost surrogate model of the system based on Kriging. Considering the spread quantities, the value of the average power in assumed frequency band can be described as

$$P_{\text{avg}} = R_{\text{L}} i_{RMS}(\mathbf{Y})^2, \tag{25}$$

where i_{RMS} is a rms value of current and depends on vector $\mathbf{Y}$ of normal distributions of the considered parameters

$$\mathbf{Y} \sim \mathcal{N}\left(\boldsymbol{\mu}, \boldsymbol{\sigma}^2\right). \tag{26}$$

where $\boldsymbol{\mu}$ and $\boldsymbol{\sigma}$ are vectors of mean values and standard deviations, given in Table 2.

The input variables for the algorithm for creating the surrogate model (see Figure 7) are the following quantities:

- geometrical and material parameters of the converter along with their standard deviations (e.g., as in Table 2)
- percentage of sample points used for validation of the surrogate model
- frequency band where the average output value is determined
- the maximum value of root-mean-square error (ε_{max}) and the maximum number of epochs ($\text{epochs}_{\text{max}}$).

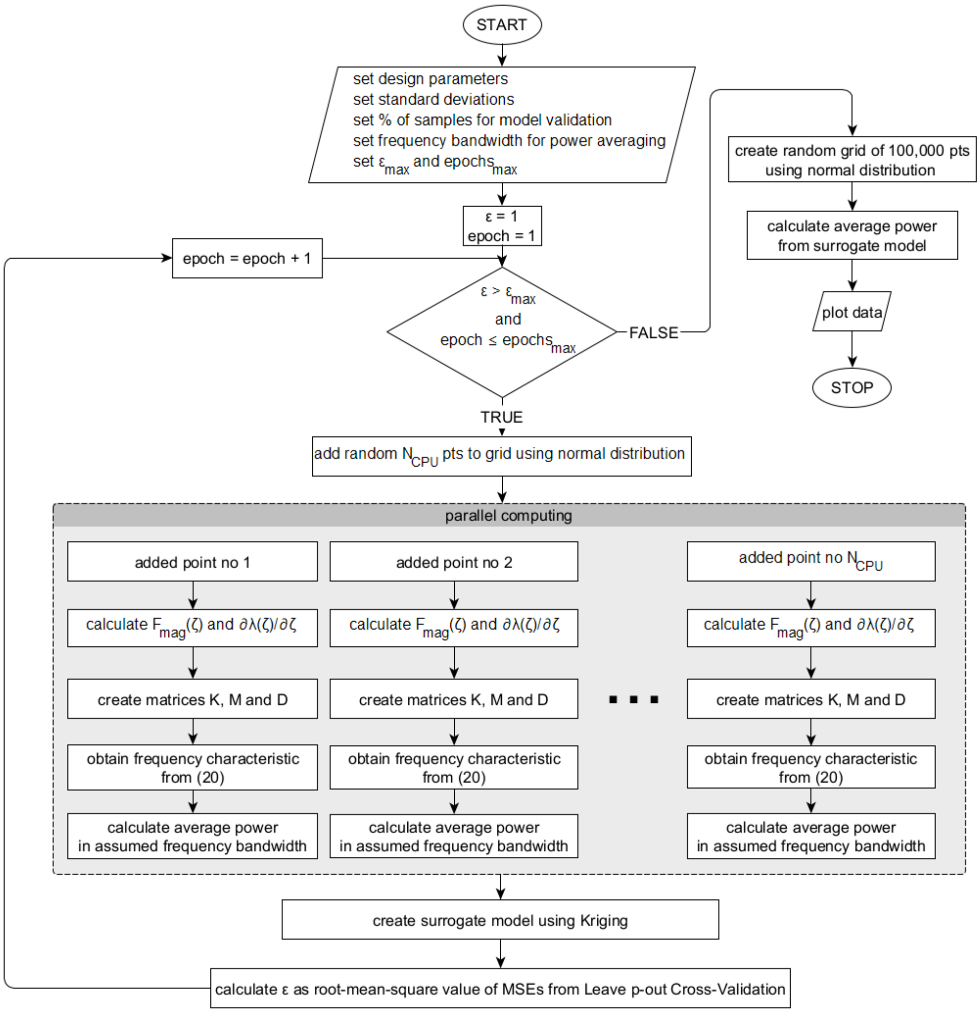

Figure 7. Flowchart diagram illustrating algorithm for creating surrogate model for fast computation of average power in assumed frequency bandwidth. N_{CPU}—number of processor cores, MSEs—mean squared errors.

In the next step, the initial error value of the surrogate model is set and a value of 1 is assigned to the epoch counter. Then, as long as the error is greater than the preset

(ε_{max}) and at the same time the epoch variable is less than or equal to the number of assumed maximum epochs ($epochs_{max}$), the simulation using (20) is performed for the design grid consisting of points generated using the normal distribution. Each point is obtained for the selected design parameters considering their standard deviations. In this way, the time-domain simulations using the mathematical models described in Section 3 can be accelerated by running them on a parallel pool. The number of additional points generated in each model correction loop increasing the metamodel accuracy is limited by the number of processor cores, N_{CPU}; however, 6–8 points per loop, available on contemporary desktop computers, is enough. These simulations are performed for a sinusoidal vibration acceleration with increasing frequency (chirp-like signal), with a frequency range that must be broader than the assumed frequency band wherein the output power has to be calculated. Once the time-series calculations are completed, the average value of the output power in the assumed frequency band is calculated. Based on the obtained powers for the randomly selected points so far, including points from previous epochs, an equivalent model is created using the Kriging method. Because this method is an interpolation-based one, at the training nodes (points), the error value will always be null [37]. To prevent overtraining the surrogate model, it is necessary to ensure that the error ε was reduced in the gaps between the training points. To do this, the Leave p-out Cross-Validation (LpO CV) method was used [49]. In this method, part of the data is not involved in training but is used to validate it. This avoids overtraining the surrogate model. The final error value of the metamodel is calculated by root-mean-square of the errors obtained from cross-validation. The surrogate model correction loop is executed until the error (ε) is below the assumed value (ε_{max}) or when the value of the epoch counter (epoch) exceeds the maximum value.

4.2. Results

The implementation of the above algorithm was carried out on a PC unit equipped with a 6-core Intel Core i7-5820K CPU @ 3.30 GHz and 24 GB RAM. Table 3 summarises the execution times of creating the surrogate model for different vibration acceleration values and the execution times required for estimation of the average output power using the created metamodel for 10^5 random design points. In addition, Table 3 provides ratios of the computer execution time reduction using the metamodel. As can be seen, the ratios are approximately equal to 333 when taking into account the time required to create the surrogate models. Neglecting the latter, the ratios are around 2×10^7. The maximum relative error assumed in calculations was 0.01, and the maximum number of epochs was set to 50. The ratio of points taken for validation was 1/6. For acceleration equal to 7.5 m/s^2, 10 m/s^2, and 12.5 m/s^2 the average output power for the frequency bands was calculated as 25–30 Hz, 30–35 Hz, and 35–40 Hz, respectively.

Table 3. Comparison of execution times for surrogate creation and those required for estimation of average output power for three different vibration accelerations.

	Process of Surrogate Model Creating (for 50 Epochs and 300 Design Grid Points)	**Average Power Evaluation from Surrogate Model (for 10^5 Points)**	**Reduction of Computation Time (10^5 Points Including the Creation Time of the Surrogate Model)**	**Reduction of Computation Time (10^5 Points Excluding the Creation Time of the Surrogate Model)**
7.5 m/s^2	37 h 27 m 40 s	1.7 s	333	2.64×10^7
10 m/s^2	32 h 06 m 32 s	1.7 s	333	2.27×10^7
12.5 m/s^2	31 h 01 m 51 s	1.7 s	333	2.19×10^7

Figure 8 shows the variation of rms errors ε vs. the learning epoch counter. As can be seen, in each case the number of epochs reached the maximum value. Achieving an error below the assumed value would require a much higher number of epochs in the process of creating the surrogate model, especially for accelerations equal to 7.5 m/s^2 and 10 m/s^2, which would require significantly higher computational cost.

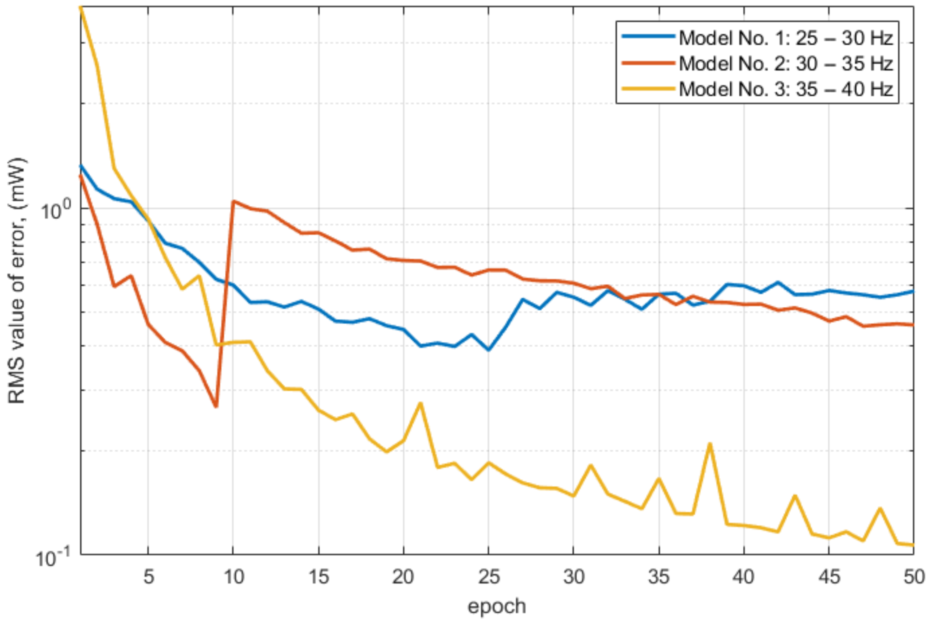

Figure 8. RMS error values ε for surrogate models vs. number of epochs.

Figures 9 and 10 show the calculated frequency characteristics of the rms voltage and power for the system loaded by the resistance equal to the resistance of the winding. These characteristics were determined in the process of creating the surrogate models for the considered vibration accelerations. As can be seen, there is a relatively large spread of results for the assumed standard deviations of the design parameters.

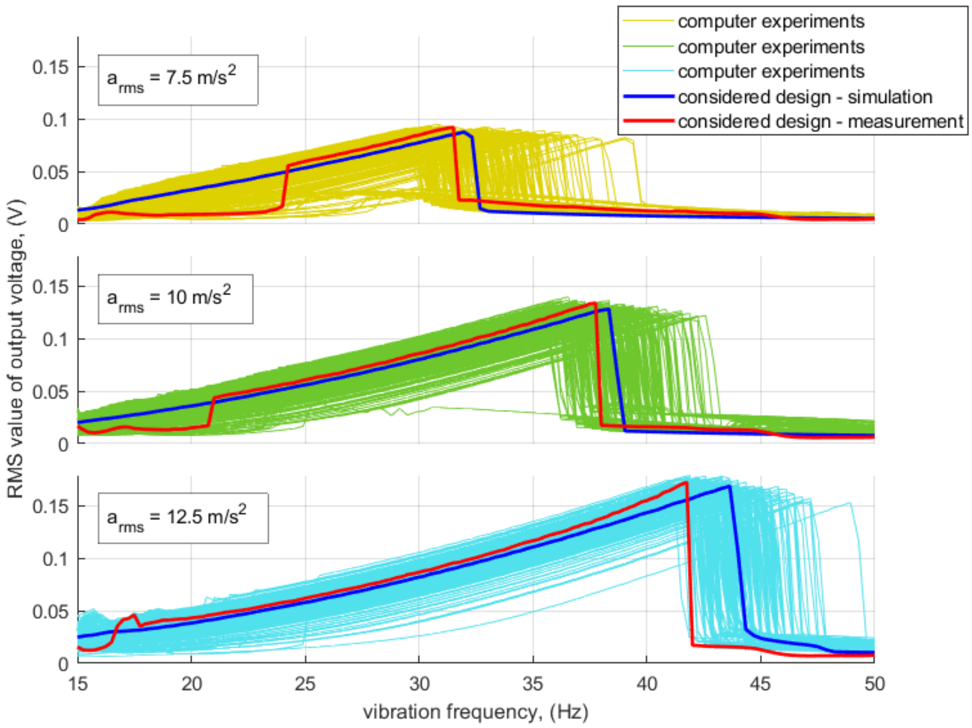

Figure 9. RMS values of output voltage vs. frequency for training points computed from full model for different RMS values of vibration accelerations.

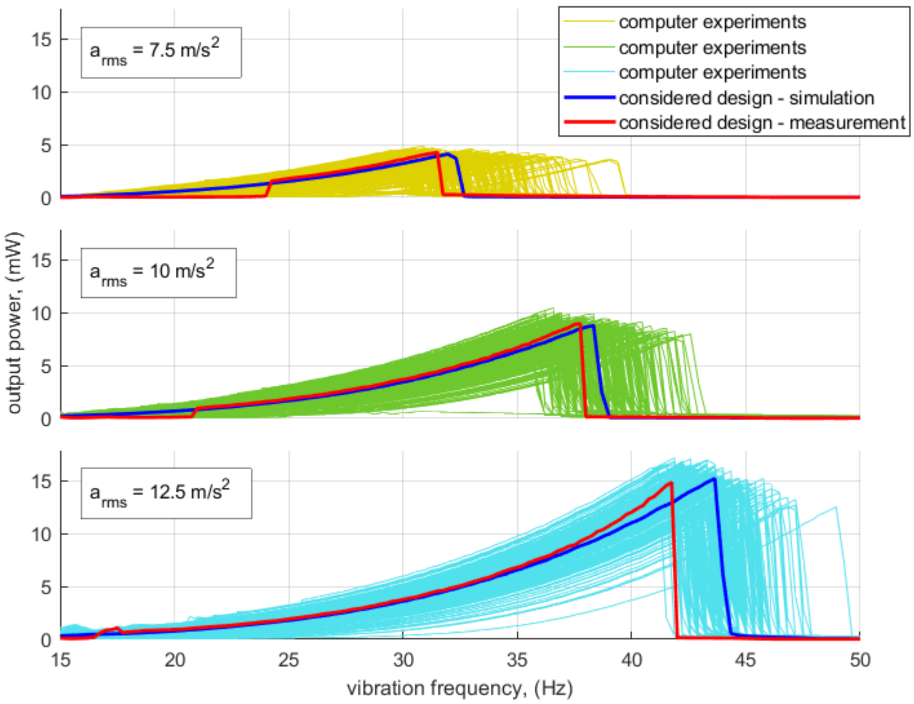

Figure 10. Output power vs. frequency for training points computed from full model for different RMS values of vibration accelerations.

The difference between the measured values and the results obtained from the simulations for the considered design appear at lower frequencies (15–24 Hz for a_{rms} = 7.5 m/s^2, 15–21 Hz for a_{rms} = 10 m/s^2 and 15–18 Hz for a_{rms}=12.5 m/s^2) and in frequency ranges at which the resonance fades out (32–33 Hz for a_{rms}= 7.5 m/s^2, 38–39 Hz for a_{rms} = 10 m/s^2 and 42–44 Hz for a_{rms} = 12.5 m/s^2). These are due to the problems in the estimation of the mechanical stiffness of the beam spring manufactured from the fibreglass composite and neglecting the effects of the complex motion of the vibrating yokes [31] by model (20).

Figures 11–13 present the values of the average output power of the system calculated from the metamodel. From the output values for the considered design, the successive levels of standard deviations of power are marked in each direction. The presented results show a large dispersion of these values for the assumed ranges of variation of material and dimensional parameters, which confirm the need for using uncertainty analysis when designing this type of converter.

Figure 11 shows the uncertainty analysis of the average output power considering only the deviations of beam dimensions. The ranges of output power calculated from the metamodel for accelerations of 7.5 m/s^2, 10 m/s^2 and 12.5 m/s^2 are 0.31–3.16 mW, 2.04–6.98 mW and 5.08–11.73 mW, respectively.

Figure 12, in contrast to Figure 11, shows the uncertainty analysis taking deviations of material parameters into account. As it can be seen, the effect of these parameters on the standard deviation of the average power is much smaller than the effect of the beam geometry. The power ranges are as follows: for acceleration of 7.5 m/s^2, from 1.62–3.04 mW; for 10 m/s^2, from 4.11–5.69 mW; and for 12.5 m/s^2, from 7.90–9.63 mW.

Figure 13 shows the uncertainty analysis with deviations of all considered parameters and dimensions. The calculations gave results that fall within the ranges 0.31–3.81 mW, 2.03–7.00 mW and 5.29–11.85 mW, for accelerations of 7.5 m/s^2, 10 m/s^2 and 12.5 m/s^2, respectively. In Figure 13, it can be seen that the power distribution for accelerations of 10 and 12.5 m/s^2 follows approximately the shape of a normal distribution of probability.

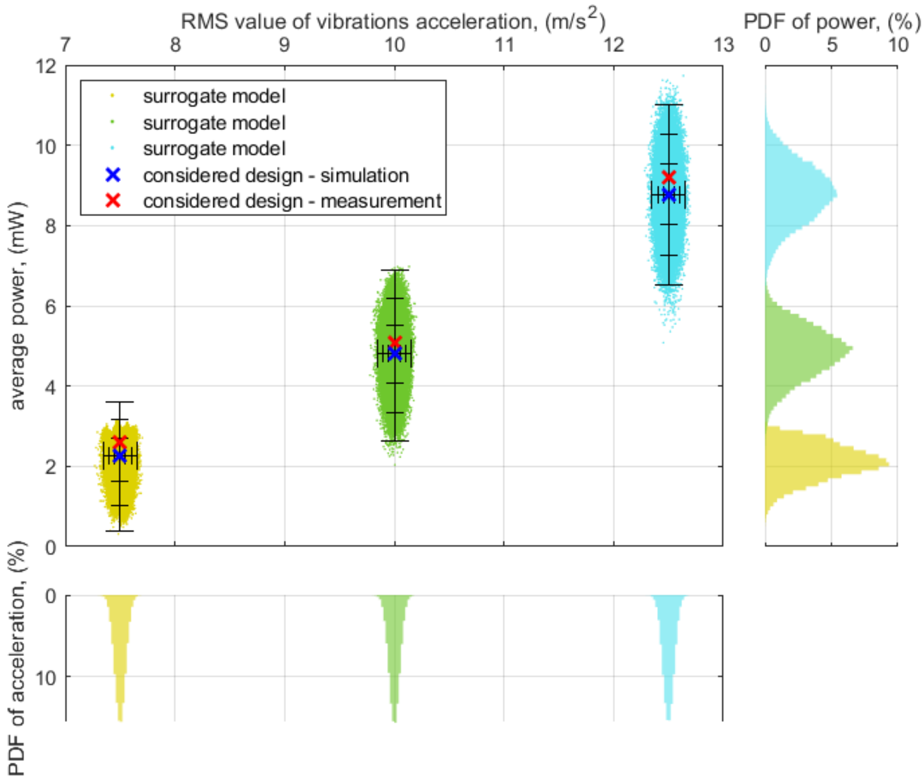

Figure 11. Average power for 10^5 design points with probability density functions (PDF) and errorbars denoting confidence levels considering only the deviations of beam dimensions.

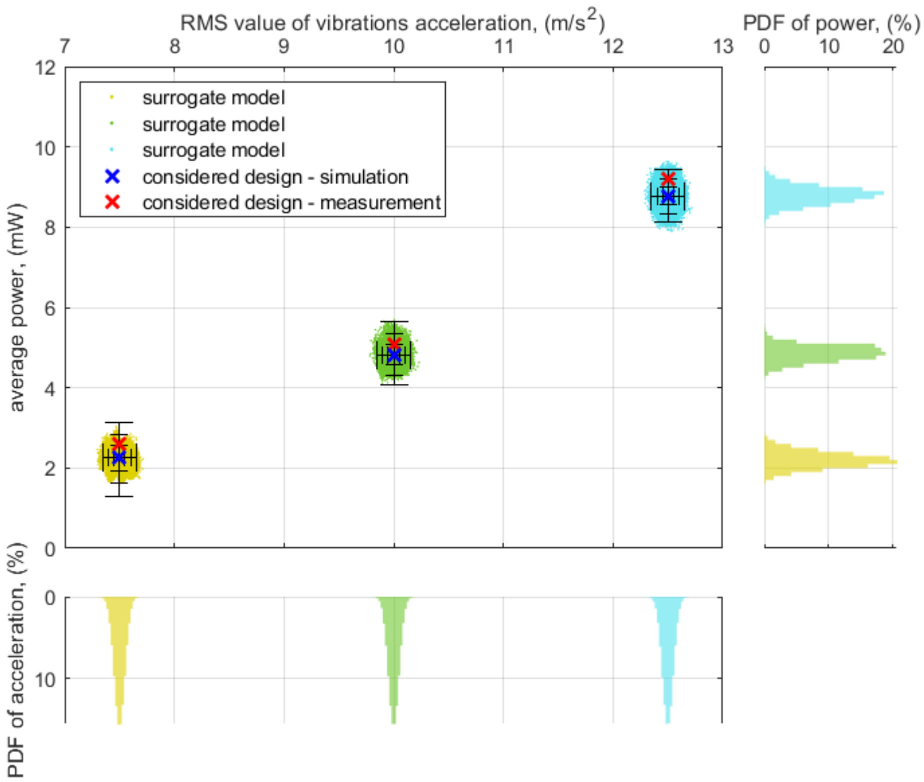

Figure 12. Average power for 10^5 design points with probability density functions (PDF) and errorbars denoting confidence levels considering only the deviations of material parameters.

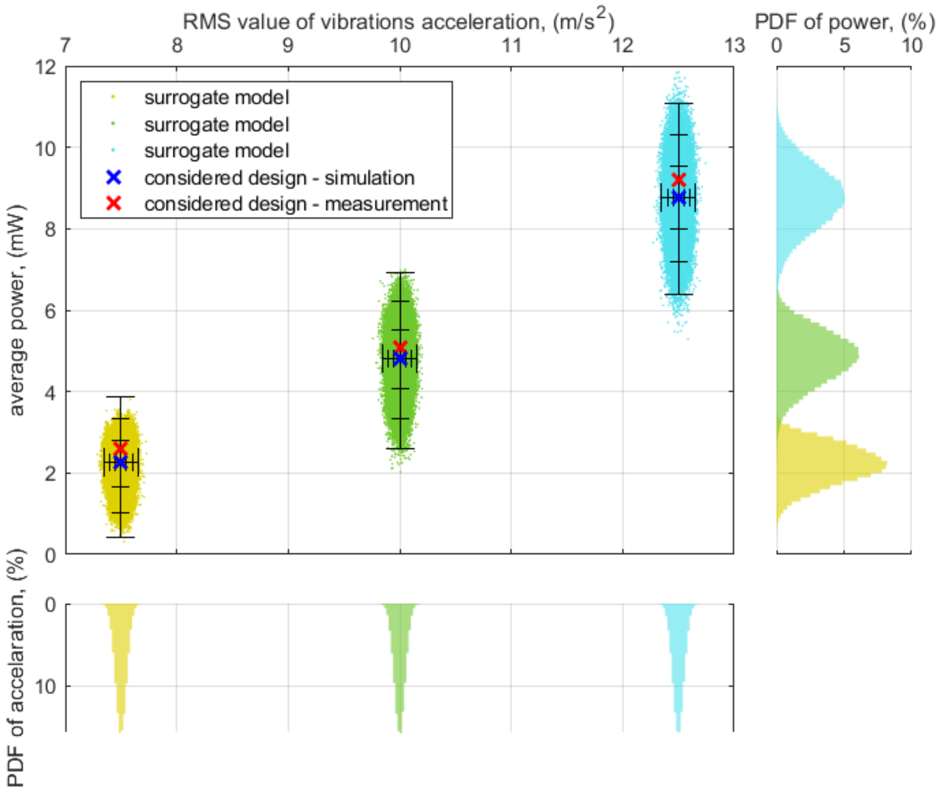

Figure 13. Average power for 10^5 design points with probability density functions (PDF) and errorbars denoting confidence levels taking into account the error of the surrogate model.

For the assumed standard deviations, the measured values of average power within the assumed frequency bands are within one confidence interval, excluding the analysis shown in Figure 12 on the effect of deviations of the material parameters only.

The proposed process of uncertainty analysis and the obtained results for the considered cases, confronted with the measurements, lead to the conclusions presented below.

5. Conclusions

- The paper proposed an algorithm for estimation of the design uncertainty of the output power of the considered electromagnetic vibration energy harvester with respect to the design parameters, namely the dimensions and the material properties.
- The metamodels created using the Kriging method enabled calculation of the average output power within the prescribed frequency band limits, significantly reducing the time of computations, which is crucial in uncertainty analysis due to the large number of time-intensive computer experiments.
- For the assumed standard deviations from the considered design for which a physical model was manufactured, one can observe high consistency of the measured frequency characteristics with the calculated ones, whilst the measured average power values are within one confidence interval.
- The use of the developed algorithm for creating the surrogate model made it possible to analyse the uncertainty of the system under consideration, which would hardly be possible using the full model presented in the paper due to the high computational cost involved.
- Future research will be conducted in the area of optimisation of the system considering the fatigue of the vibrating beam, in order to take the reliability of the converter into account in the design.
- Future research will also include analyses of the system taking into account the structure of the power converter in the formulation of the mathematical model.

The identified limitations of the proposed approach are:

- As every metamodel, it remains correct only within the range of design variables where it was trained, although in this particular system it is impossible to create a metamodel with highly accurate response in the range of operation frequency where the resonance fades out (jump in magnitude) because the physical complexity of this phenomenon is beyond the functionality of the metamodel.
- For large deviations of parameters approaching 200 per cent of those in Table 2, the error in the response provided by the surrogate model increases to unacceptably large values.

Author Contributions: Conceptualization, M.K.; Investigation, M.K. and R.G.; Methodology, M.K.; Software, M.K.; Supervision, M.J.; Visualization, M.K. and R.G.; Writing—original draft, M.K. and R.G.; Writing—review & editing, M.J. All authors have read and agreed to the published version of the manuscript.

Funding: This research was funded by The National Centre for Research and Development, Poland, grant number TANGO-V-A/0023/2021-00.

Data Availability Statement: Not applicable.

Conflicts of Interest: The authors declare no conflict of interest.

References

1. Alcácer, V.; Cruz-Machado, V. Scanning the Industry 4.0: A Literature Review on Technologies for Manufacturing Systems. *Eng. Sci. Technol. Int. J.* **2019**, *22*, 899–919. [CrossRef]
2. Baena, F.; Guarin, A.; Mora, J.; Sauza, J.; Retat, S. Learning Factory: The Path to Industry 4.0. *Procedia Manuf.* **2017**, *9*, 73–80. [CrossRef]
3. Peruzzini, M.; Grandi, F.; Pellicciari, M. Benchmarking of Tools for User Experience Analysis in Industry 4.0. *Procedia Manuf.* **2017**, *11*, 806–813. [CrossRef]
4. Xu, X.; Lu, Y.; Vogel-Heuser, B.; Wang, L. Industry 4.0 and Industry 5.0—Inception, conception and perception. *J. Manuf. Syst.* **2021**, *61*, 530–535. [CrossRef]
5. Stoppato, A.; Benato, A.; De Vanna, F. Environmental Impact of Energy Systems Integrated with Electrochemical Accumulators and Powered by Renewable Energy Sources in a Life-Cycle Perspective. *Appl. Sci.* **2021**, *11*, 2770. [CrossRef]
6. Sezer, N.; Koç, M. A comprehensive review on the state-of-the-art of piezoelectric energy harvesting. *Nano Energy* **2020**, *80*, 105567. [CrossRef]
7. Zuo, L.; Tang, X. Large-scale vibration energy harvesting. *J. Intell. Mater. Syst. Struct.* **2013**, *24*, 1405–1430. [CrossRef]
8. Mitcheson, P.D.; Yeatman, E.M.; Rao, G.K.; Holmes, A.S.; Green, T.C. Energy Harvesting From Human and Machine Motion for Wireless Electronic Devices. *Proc. IEEE* **2008**, *96*, 1457–1486. [CrossRef]
9. Yan, J.; Liu, M.; Jeong, Y.G.; Kang, W.; Li, L.; Zhao, Y.; Deng, N.; Cheng, B.; Yang, G. Performance enhancements in poly(vinylidene fluoride)-based piezoelectric nanogenerators for efficient energy harvesting. *Nano Energy* **2018**, *56*, 662–692. [CrossRef]
10. Hu, D.; Yao, M.; Fan, Y.; Ma, C.; Fan, M.; Liu, M. Strategies to achieve high performance piezoelectric nanogenerators. *Nano Energy* **2019**, *55*, 288–304. [CrossRef]
11. Zhou, J.; He, L.; Liu, L.; Yu, G.; Gu, X.; Cheng, G. Design and research of hybrid piezoelectric-electromagnetic energy harvester based on magnetic couple suction-repulsion motion and centrifugal action. *Energy Convers. Manag.* **2022**, *258*, 115504. [CrossRef]
12. Yang, K.; Abdelkefi, A.; Li, X.; Mao, Y.; Dai, L.; Wang, J. Stochastic analysis of a galloping-random wind energy harvesting performance on a buoy platform. *Energy Convers. Manag.* **2021**, *238*, 114174. [CrossRef]
13. Ahmad, I.; Hee, L.M.; Abdelrhman, A.M.; Imam, S.A.; Leong, M. Hybrid vibro-acoustic energy harvesting using electromagnetic transduction for autonomous condition monitoring system. *Energy Convers. Manag.* **2022**, *258*, 115443. [CrossRef]
14. Hou, Z.; Zha, W.; Wang, H.; Liao, W.-H.; Bowen, C.R.; Cao, J. Bistable energy harvesting backpack: Design, modeling, and experiments. *Energy Convers. Manag.* **2022**, *259*, 115441. [CrossRef]
15. Challa, V.R.; Prasad, M.G.; Shi, Y.; Fisher, F.T. A vibration energy harvesting device with bidirectional resonance frequency tunability. *Smart Mater. Struct.* **2008**, *17*, 015035. [CrossRef]
16. Won, S.S.; Seo, H.; Kawahara, M.; Glinsek, S.; Lee, J.; Kim, Y.; Jeong, C.K.; Kingon, A.I.; Kim, S.-H. Flexible vibrational energy harvesting devices using strain-engineered perovskite piezoelectric thin films. *Nano Energy* **2018**, *55*, 182–192. [CrossRef]
17. Ali, F.; Raza, W.; Li, X.; Gul, H.; Kim, K.-H. Piezoelectric energy harvesters for biomedical applications. *Nano Energy* **2019**, *57*, 879–902. [CrossRef]
18. Bowen, C.R.; Kim, H.A.; Weaver, P.M.; Dunn, S. Piezoelectric and ferroelectric materials and structures for energy harvesting applications. *Energy Environ. Sci.* **2014**, *7*, 25–44. [CrossRef]

19. Pelz, P.F.; Groche, P.; Pfetsch, M.E.; Schaeffner, M. Mastering uncertainty in mechanical engineering. In *Springer Tracts in Mechanical Engineering*; Springer: Cham, Switzerland, 2021. [CrossRef]
20. Wang, X.Q.; Liao, Y.; Mignolet, M.P. Uncertainty Analysis of Piezoelectric Vibration Energy Harvesters Using a Finite Element Level-Based Maximum Entropy Approach. *ASME* **2020**, *7*, 010906. [CrossRef]
21. Grebici, K.; Goh, Y.M.; McMahon, C. Uncertainty and risk reduction in engineering design embodiment processes. In Proceedings of the DS 48: Proceedings DESIGN 2008, the 10th International Design Conference, Dubrovnik, Croatia, 19–22 May 2008; pp. 143–156.
22. Clarkson, J.; Eckert, C. *Design Process Improvement: A Review of Current Practice*; Springer: Berlin/Heidelberg, Germany, 2005. [CrossRef]
23. Oberkampf, W.L.; DeLand, S.M.; Rutherford, B.M.; Diegert, K.V.; Alvin, K.F. Error and uncertainty in modeling and simulation. *Reliab. Eng. Syst. Saf.* **2002**, *75*, 333–357. [CrossRef]
24. Pons, D.J.; Raine, J.K. Design with uncertain qualitative variables under imperfect knowledge. *Proc. Inst. Mech. Eng. Part B J. Eng. Manuf.* **2004**, *218*, 977–986. [CrossRef]
25. Zimmermann, H.-J. An application-oriented view of modeling uncertainty. *Eur. J. Oper. Res.* **2000**, *122*, 190–198. [CrossRef]
26. Zhu, L.; Lu, H.; Zhang, Y. A system reliability estimation method by the fourth moment saddle point approximation and copula functions. *Qual. Reliab. Eng. Int.* **2021**, *37*, 2950–2969. [CrossRef]
27. Jung, H.J.; Eshghi, A.T.; Lee, S. Structural Failure Detection Using Wireless Transmission Rate From Piezoelectric Energy Harvesters. *IEEE/ASME Trans. Mechatronics* **2021**, *26*, 1708–1718. [CrossRef]
28. Nezhad, H.B.; Miri, M.; Ghasemi, M.R. New neural network-based response surface method for reliability analysis of structures. *Neural Comput. Appl.* **2019**, *31*, 777–791. [CrossRef]
29. Blokhina, E.; El Aroudi, A.; Alarcon, E.; Galayko, D. *Nonlinearity in Energy Harvesting Systems: Micro- and Nanoscale Applications*; Springer: Berlin/Heidelberg, Germany, 2016. [CrossRef]
30. Eshghi, A.T.; Lee, S.; Sadoughi, M.K.; Hu, C.; Kim, Y.-C.; Seo, J.-H. Design optimization under uncertainty and speed variability for a piezoelectric energy harvester powering a tire pressure monitoring sensor. *Smart Mater. Struct.* **2017**, *26*, 105037. [CrossRef]
31. Jagiela, M.; Kulik, M. Action of torsion and axial moment in a new nonlinear cantilever-type vibration energy harvester. *Int. J. Appl. Electromagn. Mech.* **2018**, *57* (Suppl. S1), 135–142. [CrossRef]
32. Sato, T.; Watanabe, K.; Igarashi, H. Coupled Analysis of Electromagnetic Vibration Energy Harvester With Nonlinear Oscillation. *IEEE Trans. Magn.* **2014**, *50*, 313–316. [CrossRef]
33. Noh, J.; Nguyen, M.S.; Kim, P.; Yoon, Y.-J. Harmonic balance analysis of magnetically coupled two-degree-of-freedom bistable energy harvesters. *Sci. Rep.* **2022**, *12*, 6221. [CrossRef]
34. Kreyszig, E. *Advanced Engineering Mathematics*, 10th ed.; Wiley: Hoboken, NJ, USA, 2011; pp. 154–196. ISBN 9780470458365.
35. Krack, M.; Gross, J. *Harmonic Balance for Nonlinear Vibration Problems*; Springer: Berlin/Heidelberg, Germany, 2019. [CrossRef]
36. Martins, JRRA. *; Ning, A. Engineering Design Optimization*; Cambridge University Press: Cambridge, UK, 2021; ISBN 9781108980647.
37. Forrester, A.I.J.; Sóbester, A.; Keane, A.J. *Engineering Design via Surrogate Modelling*; John Wiley & Sons, Ltd.: Hoboken, NJ, USA, 2008.
38. Kulik, M.; Jagieła, M.; Łukaniszyn, M. Surrogacy-Based Maximization of Output Power of a Low-Voltage Vibration Energy Harvesting Device. *Appl. Sci.* **2020**, *10*, 2484. [CrossRef]
39. Jagieł, M.; Kulik, M. Wideband Electromagnetic Converter of Mechanical Vibrations Energy into Electrical Energy. Patent Office of the Republic of Poland. No. Pat. 239301, 27 March 2017. (In Polish)
40. Jin, S.-S.; Jung, H.-J. Sequential surrogate modeling for efficient finite element model updating. *Comput. Struct.* **2016**, *168*, 30–45. [CrossRef]
41. Rakotoarison, H.; Yonnet, J.; Delinchant, B. Using Coulombian approach for Modeling Scalar Potential and Magnetic Field of a Permanent Magnet with Radial Polarization. *IEEE Trans. Magn.* **2007**, *43*, 438. [CrossRef]
42. Ravaud, R.; Lemarquand, G.; Lemarquand, V.; Depollier, C. Discussion about the analytical calculation of the magnetic field created by permanent magnets. *Prog. Electromagn. Res. B* **2009**, *11*, 281–297. [CrossRef]
43. Riley, K.F.; Hobson, M.P.; Bence, S.J.; Spector, D. Mathematical Methods for Physics and Engineering. *Am. J. Phys.* **1999**, *67*, 165–169. [CrossRef]
44. Akyel, C.; Babic, S.; Kincic, S. New and fast procedures for calculating the mutual inductance of coaxial circular coils (circular coil-disk coil). *IEEE Trans. Magn.* **2002**, *38*, 2367–2369. [CrossRef]
45. Yu, D.; Han, K. Self-inductance of air-core circular coils with rectangular cross section. *IEEE Trans. Magn.* **1987**, *23*, 3916–3921. [CrossRef]
46. Zierhofer, C.; Hochmair, E. Geometric approach for coupling enhancement of magnetically coupled coils. *IEEE Trans. Biomed. Eng.* **1996**, *43*, 708–714. [CrossRef]
47. Akoun, G.; Yonnet, J.-P. 3D analytical calculation of the forces exerted between two cuboidal magnets. *IEEE Trans. Magn.* **1984**, *20*, 1962–1964. [CrossRef]
48. Ferreira, A.J.M. Matlab codes for finite element analysis. In *Solid Mechanics and Its Applications 157*; Springer: Berlin/Heidelberg, Germany, 2009; ISBN 978-1-4020-9199-5.
49. Bruton, S.L.; Kutz, J.N. *Data-Driven Science and Engineering: Machine Learning, Dynamical Systems, and Control*; Cambridge University Press: Cambridge, UK, 2019.